Journal of Power Sources 247 (2014) 778–785

Contents lists available at ScienceDirect

Journal of Power Sources

journal homepage: www.elsevier.com/locate/jpowsour

# Enhanced rate performance of molybdenum-doped spinel $LiNi_{0.5}Mn_{1.5}O_4$ cathode materials for lithium ion battery

Ting-Feng Yi [a, b, c, *], Bin Chen [a], Yan-Rong Zhu [a], Xiao-Ya Li [a], Rong-Sun Zhu [a]

[a] School of Chemistry and Chemical Engineering, Anhui University of Technology, Maanshan, Anhui 243002, People's Republic of China
[b] Postdoctoral Research Station of Chemical Engineering & Technology, Harbin Institute of Technology, 150001 Harbin, People's Republic of China
[c] Chilwee Power Co. Ltd., Changxing, Zhejiang 313100, People's Republic of China

## HIGHLIGHTS

- Mo-doped $LiNi_{0.5}Mn_{1.5}O_4$ cathode is first reported.
- Mo doped $LiNi_{0.5}Mn_{1.5}O_4$ shows high lithium diffusion coefficient and good rate capability.
- $LiMn_{1.4}Ni_{0.55}Mo_{0.05}O_4$ shows a potential advantage for high power battery applications.

## ARTICLE INFO

*Article history:*
Received 31 May 2013
Received in revised form
30 August 2013
Accepted 6 September 2013
Available online 17 September 2013

*Keywords:*
Lithium-ion battery
Cathode material
Rate capability
Lithium manganese oxide
Doping

## ABSTRACT

The Mo-doped $LiNi_{0.5}Mn_{1.5}O_4$ cathodes are successfully synthesized by citric acid-assisted sol–gel method. The result demonstrates that the Mo-doped $LiMn_{1.4}Ni_{0.55}Mo_{0.05}O_4$ cathodes present the improved electrochemical performance over pristine $LiNi_{0.5}Mn_{1.5}O_4$. At the 2 C rate after 80 cycles, the discharge capacities are 68.5 mAh $g^{-1}$ for the pristine $LiNi_{0.5}Mn_{1.5}O_4$ material (53.9% of the capacity at 0.1 C), 107.4 mAh $g^{-1}$ for the $LiMn_{1.425}Ni_{0.5}Mo_{0.05}O_4$ material (82.1% at 0.1 C), and 122.7 mAh $g^{-1}$ for the $LiMn_{1.4}Ni_{0.55}Mo_{0.05}O_4$ material (90.5% at 0.1 C). Mo-doping is favorable for reducing the electrode polarization, suggesting that Mo-doped $LiNi_{0.5}Mn_{1.5}O_4$ electrodes have faster lithium insertion/extraction kinetics during cycling. Mo-doped $LiNi_{0.5}Mn_{1.5}O_4$ electrodes show lower charge-transfer resistance and higher lithium diffusion coefficients. In addition, $LiMn_{1.4}Ni_{0.55}Mo_{0.05}O_4$ cathode exhibits the smallest particle size, the lowest charge-transfer resistance and the highest lithium diffusion coefficient among all samples, indicating that it has a high reversibility and good rate capability.



## 1. Introduction

Lithium-ion batteries have great potential as a new large-scale power source for electric vehicles (EVs), hybrid electrical vehicles (HEVs), and plug-in hybrid vehicles (PHEVs) due to their high energy density, high voltage, and long cycle life [1–3]. However, a further improvement in terms of safety, cycling life and, particularly, energy density is still required to fulfill the demands of these applications [4]. At present, spinel lithium manganese oxide ($LiMn_2O_4$) is one of the most sought-after cathode owing to its adequate capacity, economical production, safety, low toxicity and high thermal stability [5]. However, poor rate capability, cyclability and high-temperature performance limit its further application for high-performance rechargeable batteries due to the Jahn–Teller distortion of the structure and the slow dissolution of manganese resulting from the disproportionate reactions of $Mn^{3+}$ ($2Mn^{3+} \rightarrow Mn^{2+} + Mn^{4+}$) in the presence of acidic species in an electrolyte [6–8]. Quaternary spinels of the general formula $LiM_xMn_{2-x}O_4$ (M = Cr, Co, Ni, Al, etc) were able to alleviate the capacity fade of the cathode upon cycling [9–12]. Among all doped $LiM_xMn_{2-x}O_4$, $LiNi_{0.5}Mn_{1.5}O_4$ and its variants have been attracted much intensive interest due to its high discharge capacity and attractive voltage plateau. In $LiNi_{0.5}Mn_{1.5}O_4$, the redox process occurs on the Ni site only, which prevents the creation of the $Mn^{3+}$ cation and its related problems [13]. The new spinel cathode material $LiNi_{0.5}Mn_{1.5}O_4$ exhibits a high potential of about 4.7 V (versus $Li/Li^+$), which increases the total energy density of $LiNi_{0.5}Mn_{1.5}O_4$ as compared to $LiMn_2O_4$ from 440 Wh $kg^{-1}$ to 686 Wh $kg^{-1}$ [14]. Unfortunately, the poor responses in the discharge capacity and cyclability of $LiNi_{0.5}Mn_{1.5}O_4$ at large current hinder its feasible

* Corresponding author. School of Chemistry and Chemical Engineering, Anhui University of Technology, Maanshan, Anhui 243002, People's Republic of China. Tel.: +86 555 2311807; fax: +86 555 2311822.
*E-mail address:* tfyihit@163.com (T.-F. Yi).

0378-7753/$ – see front matter © 2013 Elsevier B.V. All rights reserved.
http://dx.doi.org/10.1016/j.jpowsour.2013.09.031

application. One of the reasons is that the $LiNi_{0.5}Mn_{1.5}O_4$ loses oxygen and disproportionates to a spinel and $Li_xNi_{1-x}O$ or NiO prepared above 650 °C. Hence, $LiNi_{0.5}Mn_{1.5}O_4$ still has a non-negligible capacity fading during cycling due to the structural and chemical instabilities resulted from the presence of high spin $Mn^{3+}$ ions. Cations or anions doping have been considered to be effective ways to improve the intrinsic properties of $LiNi_{0.5}Mn_{1.5}O_4$ materials. The doped cations and anions include $Mg^{2+}$ [15], $Cr^{3+}$ [16], $Co^{3+}$ [17], $Fe^{3+}$ [18], $Ru^{4+}$ [19], $Nb^{5+}$ [20], $F^-$ [21] and $S^{2-}$ [22]. To our knowledge, the rate cycling performance of $Mo^{6+}$-doped $LiNi_{0.5}Mn_{1.5}O_4$ was not reported. Hence, the designed compositions of Mo-doped $LiNi_{0.5}Mn_{1.5}O_4$ spinels are $Mn^{4+}$, $Ni^{2+}$ and $Mo^{6+}$. The charge–discharge capacity of $LiNi_{0.5}Mn_{1.5}O_4$ is from the reversible redox reactions between bivalent nickel ion ($Ni^{2+}$) and tetravalent nickel ion ($Ni^{4+}$). Hence, the amount of $Ni^{2+}$ determines the capacity of $LiNi_{0.5}Mn_{1.5}O_4$. Strobel et al. [23] reported that XRD pattern of freshly prepared $LiMnCoO_4$ shows that it is not a single-phase. The data can be ascribed to a majority $LiMO_2$-type layered phase and a minority spinel one. Hence, it can be concluded that the Mn element has a supporting role of the spinel framework in the spinel lithium manganese oxide. With this consideration, we hope that the content of Mn is not too low in the Mo-doped $LiNi_{0.5}Mn_{1.5}O_4$ spinels. Hence, we design the chemical formula of Mo-doped $LiNi_{0.5}Mn_{1.5}O_4$ spinel are $LiMn_{1.4}Ni_{0.55}Mo_{0.05}O_4$ and $LiMn_{1.425}Ni_{0.5}Mo_{0.05}O_4$. Hence, Mo-doped $LiMn_{1.5}Ni_{0.5}O_4$ compound was prepared by sol–gel method. The electrochemical performances of Mo-doped $LiMn_{1.5}Ni_{0.5}O_4$, including cycling stability and rate capability, were extensively evaluated in half cells.

## 2. Experimental

### 2.1. Material preparation

The synthesis route of $LiNi_{0.5}Mn_{1.5}O_4$, $LiMn_{1.4}Ni_{0.55}Mo_{0.05}O_4$ and $LiMn_{1.425}Ni_{0.5}Mo_{0.05}O_4$ powders synthesized by a citric acid-assisted sol–gel method was described as follows: The stoichiometric amounts of $LiCH_3COO$, $Mn(CH_3COO)_2{\cdot}4H_2O$, $Ni(CH_3COO)_2{\cdot}4H_2O$ and $(NH_4)_6Mo_7O_{24}{\cdot}4H_2O$ were initially dissolved in certain amounts of distilled water. The above mixed solution was added drop wise to the citric acid solution with continuous stirring, and the molar ratio of citric acid to total metal cations was fixed at 1:1. The pH of the mixed solution was adjusted to 7 by adding $NH_3{\cdot}H_2O$ (AR, 25%). The mixed solution was then heated with continuous stirring up to boiling point until a gel was obtained. The resulted gel was dried at 90 °C for 24 h in vacuum oven. The precursor powder was ground to fine powder and sintered at 450 °C under air flowing conditions with a constant heating followed by cooling at rate 5 °C $min^{-1}$ to decompose organic constituents. The sintered powder was ground to a fine powder and re-sintered successively at 850 °C for 18 h and heating and cooling rate was maintained at 5 °C $min^{-1}$.

### 2.2. Material characterization

Differential thermal analysis (DTA) and thermogravimetry (TG) measurements were performed in air from room temperature to 820 °C with a Henjiu Chare Tianping-1/2 thermal analysis system (Beijing, China) under a scanning rate of 5 °C $min^{-1}$. Powder X-ray diffraction (XRD, Rigaku instrument) measurements using Cu Kα radiation were employed to identify the crystalline phase of the synthesized materials. The particle morphology of the powders after sintering was obtained using a scanning electron microscopy (SEM). Cyclic voltammetry (CV) test was carried out on a PARSTAT 4000 electrochemical workstation with a voltage between 3.3 and 5.0 V at a scanning rate of 0.2 mV $s^{-1}$. Electrochemical impedance spectroscopy (EIS) is measured by a PARSTAT 4000 electrochemical working station over a frequency range from 0.1 Hz to 10 kHz at a potentiostatic signal amplitude of 5 mV. EIS measurement performed at open circuit voltage (about 3.2 V). The prepared electrode materials were adopted as the work electrode; the counter electrode and reference electrode were Li foil. The charge–discharge measurements were recorded on multichannel Land Battery Test System (Wuhan Jinnuo, China) at room temperature in 3.3–4.95 V (versus $Li/Li^+$) range. The charge measurements were carried out at 0.1 C rate, but the discharge measurements were carried out at different C-rates.

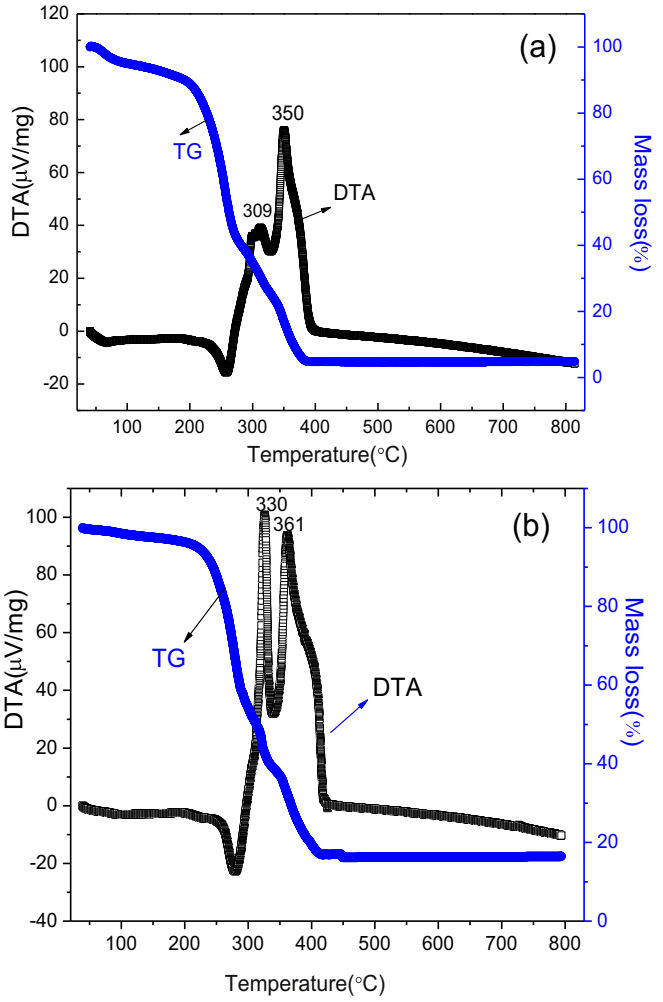


**Fig. 1.** TG–DTA curves for the thermal decomposition of the precursors of (a) $LiMn_{1.5}Ni_{0.5}O_4$, (b) $LiMn_{1.425}Ni_{0.5}Mo_{0.05}O_4$.

### 2.3. Battery preparation

Electrochemical characterizations were performed using a CR2025 coin-type cell. The cathode was prepared by mixing above active material, carbon black and polyvinylidene fluoride (PVDF) in a weight ratio of (80:10:10) and emulsified in *N*-methylpyrolline. The resulting paste was spread on aluminum foil and dried overnight at about 120 °C. The mass of electrodes for final coin cells is about 2.5 mg. The coin cell was prepared in an Ar atmosphere inside a glove box (Etelux, China) using Li metal foil as anode and

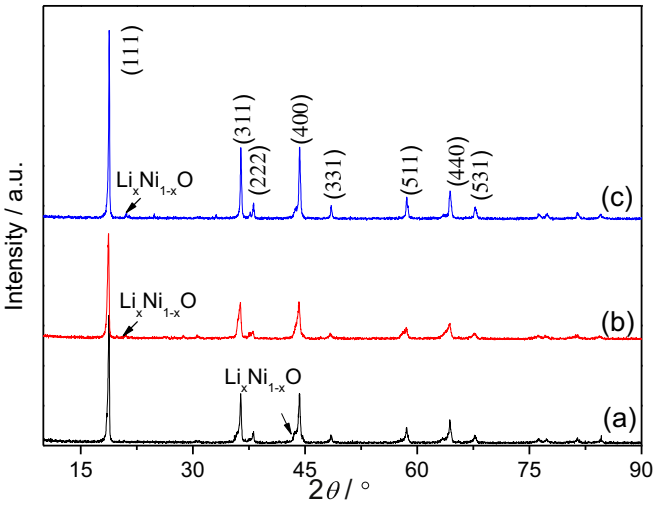


**Fig. 2.** XRD patterns of the pure and the Mo-doped $LiMn_{1.5}Ni_{0.5}O_4$ cathode materials (a) $LiMn_{1.5}Ni_{0.5}O_4$, (b) $LiMn_{1.425}Ni_{0.5}Mo_{0.05}O_4$, (c) $LiMn_{1.4}Ni_{0.55}Mo_{0.05}O_4$.

electrolyte consisting of 1 M $LiPF_6$, dissolved in ethylene carbonate and diethyl carbonate (1:1 volume ratio). The working electrode and Li metal foil were separated using Celgard polypropylene separator.

## 3. Results and discussion

Fig. 1 shows the TG–DTA results of $LiNi_{0.5}Mn_{1.5}O_4$ and $LiMn_{1.425}Ni_{0.5}Mo_{0.05}O_4$ precursors obtained by using citric acid combinations. It can be seen that the mass loss of the gel precursor occurs in three steps, at 20–200, 200–400 °C and terminates at 400 °C. The mass loss in the temperature range of 20–200 °C corresponds to the removal of superficial water, ammonia and crystal water on the gel precursor. As the process of heating is continued, the mass loss increases, owing to the combustion nature of the citric acid gel precursor. The huge mass loss in the temperature range of 200–400 °C is associated with the combustion nature of inorganic and organic constituents of the precursor such as acetate and citric acid accompanied by exothermic peaks at around 309 and 350 °C in the DTA curve. The weight is nearly constant when the temperature is above 400 °C. This indicates that the decomposition of precursor completed at about 400 °C. In a typical citric acid-assisted sol–gel process, the citric acid used as a chelating agent can release a large amount of heat during combustion and improve the crystallization reaction. It appears that citric acid functions as a fuel in the decomposition of the acetate ions and heat evolved from the decomposition of acetate ions accelerates the decomposition of the remaining organic constituents. In Fig. 1b, the exothermic peak at 330 and 361 °C is related to the decomposition of acetate and ammonium molybdate. It corresponds to the following reaction

$$\begin{aligned} &LiCH_3COO + 1.425Mn(CH_3COO)_2\cdot 4H_2O \\ &+ \frac{0.05}{7}(NH_4)_6Mo_7O_{24}\cdot 4H_2O + 10.4125O_2 \\ &+ 0.5Ni(CH_3COO)_2\cdot 4H_2O \rightarrow LiMn_{1.425}Ni_{0.5}Mo_{0.05}O_4 \\ &+ \frac{0.3}{7}NH_3 + 9.7CO_2 + 15.025H_2O \end{aligned} \quad (1)$$

This indicates that the Mo doping does not change the reaction mechanism, but the phase transition reaction temperature increases due to the Mo doping.

The synthesis condition of Mo-doped $LiNi_{0.5}Mn_{1.5}O_4$ in the present paper is in air, and the molybdenum ion tends to be $Mo^{6+}$ that may incorporate into targeted phases of $LiMn_{1.425}Ni_{0.5}Mo_{0.05}O_4$ and $LiMn_{1.4}Ni_{0.55}Mo_{0.05}O_4$. The X-ray patterns of the prepared samples are shown in Fig. 2. It can be observed from Fig. 2 that all the characteristic diffraction peaks could be assigned to a cubic spinel structure of $LiNi_{0.5}Mn_{1.5}O_4$ (PDF 80-2162) with the space group of Fd-3m. It can be concluded that Mo fully substituted for Ni and Mn [24]. However, it can be found one impurity peak at about 21–32.5° and 43.5° for pristine and Mo-doped $LiNi_{0.5}Mn_{1.5}O_4$, being recognized as the weak impurity phase of $Li_xNi_{1-x}O$. This is caused by oxygen loss when the sintering temperature was above 650 °C, accompanied with a small amount $Mn^{3+}$ generated. All fundamental peaks are sharp, which indicates that the prepared powders are well crystallized. This means that the low dose doping of $Mo^{6+}$ cannot change the basic $LiNi_{0.5}Mn_{1.5}O_4$ structure, and form a solid solution. The absence of the (2 2 0) diffraction peak around $2\theta = 30°$ indicates that there is no transition metal ions in the 8a tetrahedral positions. The lattice parameters were calculated through the least square program method from the diffraction data of $LiMn_{1.425}Ni_{0.5}Mo_{0.05}O_4$ and $LiMn_{1.4}Ni_{0.55}Mo_{0.05}O_4$, and were found to be about 8.212 and 8.186 Å, respectively, which is slightly larger than that of a pristine $LiNi_{0.5}Mn_{1.5}O_4$ positive-electrode material (8.184 Å). This fact indicates that the lattice parameters of the Mo-doped $LiNi_{0.5}Mn_{1.5}O_4$ materials are slightly larger than that for the pristine $LiNi_{0.5}Mn_{1.5}O_4$. These variations are attributed to the ionic radius differences among $Li^+$ (0.59 Å), $Ni^{2+}$ (0.69 Å), $Mn^{4+}$ (0.53 Å), and $Mo^{6+}$ (0.59 Å). $LiMn_{1.425}Ni_{0.5}Mo_{0.05}O_4$ has a larger lattice parameter than that of $LiMn_{1.4}Ni_{0.55}Mo_{0.05}O_4$, and the expansion of lattice parameter is attributed to the bigger ionic radius of $Mn^{3+}$ (0.65 Å) rather than $Mn^{4+}$ (0.53 Å). It can be found that there is a higher content of $Mn^{3+}$ in $LiMn_{1.425}Ni_{0.5}Mo_{0.05}O_4$ than that in

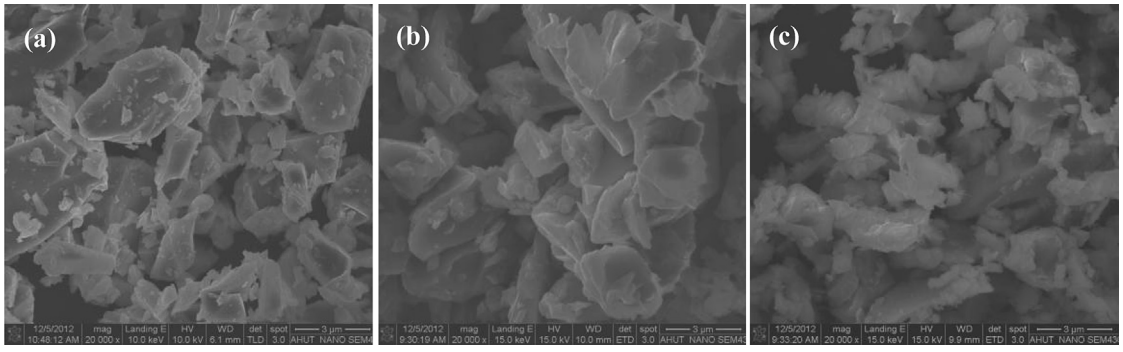


**Fig. 3.** SEM images of the pure and the Mo-doped $LiMn_{1.5}Ni_{0.5}O_4$ cathode materials (a) $LiMn_{1.5}Ni_{0.5}O_4$, (b) $LiMn_{1.425}Ni_{0.5}Mo_{0.05}O_4$, (c) $LiMn_{1.4}Ni_{0.55}Mo_{0.05}O_4$.

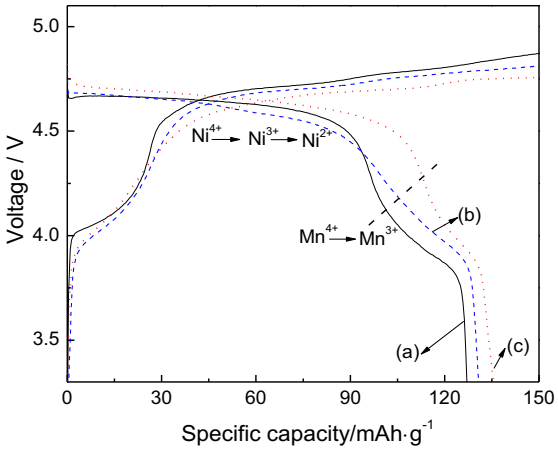


**Fig. 4.** Initial charge–discharge curves of the Mo-doped $LiNi_{0.5}Mn_{1.5}O_4$ cathode materials (a) $LiNi_{0.5}Mn_{1.5}O_4$, (b) Li $Ni_{0.5}Mn_{1.425}Mo_{0.05}O_4$, (c) $LiNi_{0.55}Mn_{1.4}Mo_{0.05}O_4$.

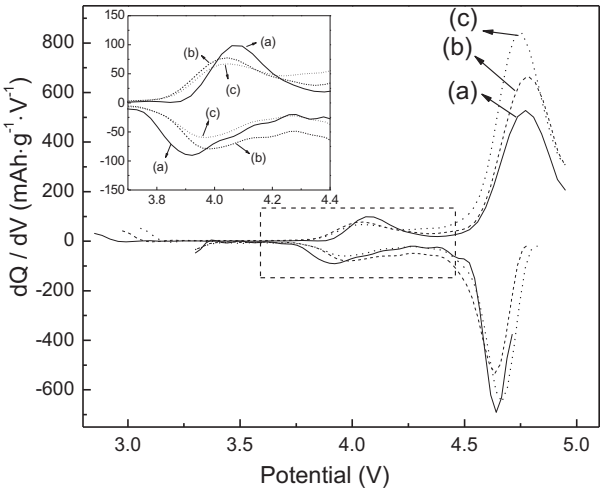


**Fig. 5.** The d$Q$/d$V$ versus voltage curves of the Mo-doped $LiMn_{1.5}Ni_{0.5}O_4$ cathode materials from Fig. 4 (a) $LiMn_{1.5}Ni_{0.5}O_4$, (b) $LiMn_{1.425}Ni_{0.5}Mo_{0.05}O_4$, (c) $LiMn_{1.4}Ni_{0.55}Mo_{0.05}O_4$.

$LiMn_{1.4}Ni_{0.55}Mo_{0.05}O_4$ according to the area of $Mn^{4+}/Mn^{3+}$ peak (shown in Fig. 5b and c).

Fig. 3 shows the SEM micrographs of the $LiNi_{0.5}Mn_{1.5}O_4$ powders with and without substitution. All morphologies of the particles are similar and the particle sizes are ranging between 3 and 5 μm for the prepared samples. Hence, it can be concluded that the particle size effect on the electrochemical properties of the samples is relatively small. These observations indicate that the doping of small amount of Mo do not significantly affect the morphology and size of the $LiNi_{0.5}Mn_{1.5}O_4$. From this point of view, the particle size effect on the electrochemical properties of the samples can be ruled out and the dissimilarity, in term of performance, of the samples can be considered to be mainly attributed to the Mo-substitution.

Fig. 4 shows the initial charge–discharge characteristics of pristine and Mo-doped $LiNi_{0.5}Mn_{1.5}O_4$, carried out at room temperature in 3.3–4.95 V range, at a current density of 0.1 $C$. It can be seen that the initial discharge capacities of $LiNi_{0.5}Mn_{1.5}O_4$, $LiMn_{1.425}Ni_{0.5}Mo_{0.05}O_4$ and $LiMn_{1.4}Ni_{0.55}Mo_{0.05}O_4$ cathode material are 127.1, 130.8 and 135.6 mAh $g^{-1}$, respectively. As expected, at the 0.1 C rate, $LiMn_{1.4}Ni_{0.55}Mo_{0.05}O_4$ exhibits the highest discharge capacity due to the highest content of $Ni^{2+}$. The irreversibility in first cycle may be due to the formation of solid electrolyte interface (SEI) layer onto the spinel [25] and the considerable electrolyte decomposition at high voltage [26]. It can be found that $LiMn_{1.4}Ni_{0.55}Mo_{0.05}O_4$ has a higher discharge plateau at about 4.7 V than that of pristine $LiMn_{1.5}Ni_{0.5}O_4$, indicating that the former has a higher power density than that of pristine $LiNi_{0.5}Mn_{1.5}O_4$. Fig. 5 shows the differential chronopotentiometry test result (d$Q$/d$V$). There is an oxidation peaks at about 4.75 V and the corresponding reduction peak at 4.65 V. This is an oxidation/reduction process of $Ni^{2+}/Ni^{4+}$. There is also a small peak at around 4.0 V, indicating that the oxidation/reduction process of $Mn^{3+}/Mn^{4+}$ exits. The $Mn^{3+}$ ions are resulted from oxygen deficiency in the high temperature sintering process. The inset in Fig. 5 is the enlarged peak of $Mn^{3+}/Mn^{4+}$ corresponding to the discharge plateaus at about 4.0 V. It can be found that the discharge curve of pristine $LiNi_{0.5}Mn_{1.5}O_4$ presents a much more obvious plateau in the potential region around 4.0 V (from the redox couples $Mn^{3+}/Mn^{4+}$), which means that the oxygen deficiency is more severe due to the oxygen loss at high calcination temperature for long reaction time. It is obvious that $LiMn_{1.4}Ni_{0.55}Mo_{0.05}O_4$ exhibits the smallest potential plateau around 4.0 V, indicating that there is a reduced content of $Mn^{3+}$ in our designed Mo-doped $LiNi_{0.5}Mn_{1.5}O_4$ samples. In addition, the charge–discharge capacity of $LiNi_{0.5}Mn_{1.5}O_4$ is from the reversible redox reactions between bivalent nickel ion ($Ni^{2+}$) and tetravalent nickel ion ($Ni^{4+}$). Hence, the amount of $Ni^{2+}$ determines the capacity of $LiNi_{0.5}Mn_{1.5}O_4$. $LiMn_{1.4}Ni_{0.55}Mo_{0.05}O_4$ has the highest content of $Ni^{2+}$ among all samples, and shows the highest discharge capacity among all samples. From Figs. 4 and 5, it can be found that $LiMn_{1.4}Ni_{0.55}Mo_{0.05}O_4$ shows the largest discharge plateau at 4.7 V among all sample. From Fig. 5, according to the area of $Ni^{4+}/Ni^{2+}$ peak at 4.7 V, it can be concluded that $LiMn_{1.4}Ni_{0.55}Mo_{0.05}O_4$ shows the largest discharge capacity at 4.7 V among all sample. The energy density can be calculated by the equation,

$$E = C \times U \quad (2)$$

where $E$ is the energy density, $C$ the discharge specific capacity, and $U$ is the voltage of the cell. $LiMn_{1.4}Ni_{0.55}Mo_{0.05}O_4$ shows the higher discharge capacity and discharge plateau at 4.7 V than those of pristine $LiNi_{0.5}Mn_{1.5}O_4$. Therefore, the energy density of

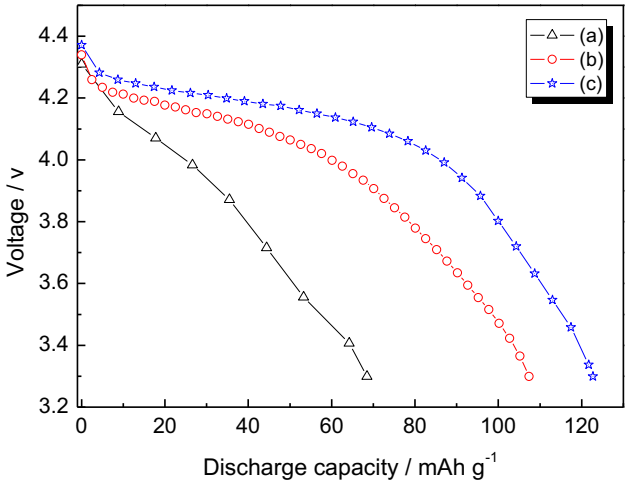


**Fig. 6.** Discharge curves of the pristine and the Mo-doped $LiMn_{1.5}Ni_{0.5}O_4$ cathode materials at the 80th cycles discharged 2 C rate. (a) $LiMn_{1.5}Ni_{0.5}O_4$; (b) $LiMn_{1.425}Ni_{0.5}Mo_{0.05}O_4$; (c) $LiMn_{1.4}Ni_{0.55}Mo_{0.05}O_4$.

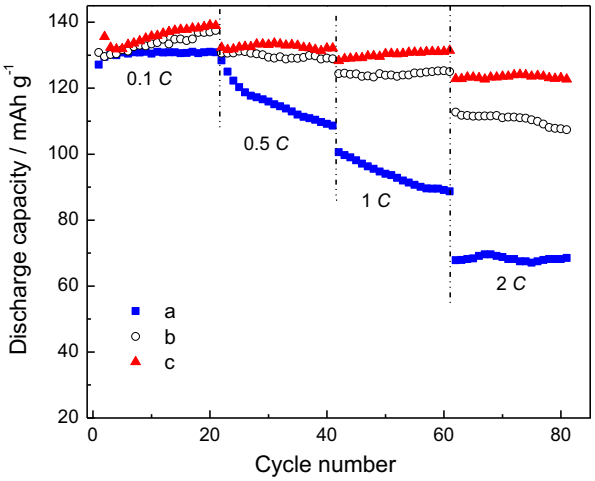


**Fig. 7.** Rate performance of the pristine and the Mo-doped $LiMn_{1.5}Ni_{0.5}O_4$ cathode materials. (a) $LiMn_{1.5}Ni_{0.5}O_4$; (b) $LiMn_{1.425}Ni_{0.5}Mo_{0.05}O_4$; (c) $LiMn_{1.4}Ni_{0.55}Mo_{0.05}O_4$.

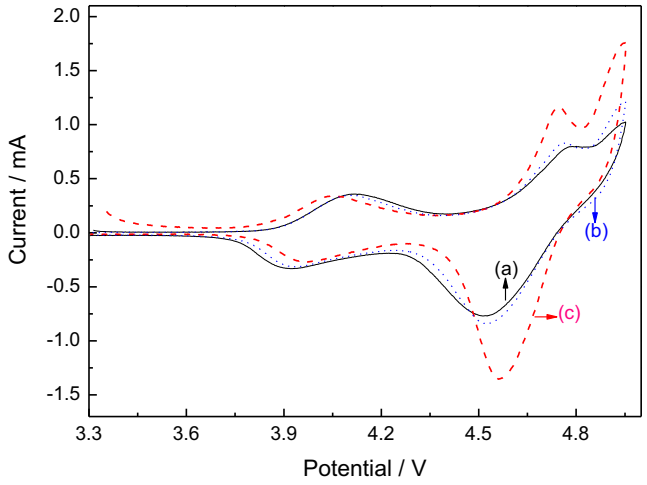


**Fig. 8.** Cyclic voltammetry (CV) of the pristine and the Mo-doped $LiMn_{1.5}Ni_{0.5}O_4$ cathode materials (a) $LiMn_{1.5}Ni_{0.5}O_4$; (b) $LiMn_{1.425}Ni_{0.5}Mo_{0.05}O_4$ and (c) $LiMn_{1.4}Ni_{0.55}Mo_{0.05}O_4$.

$LiMn_{1.4}Ni_{0.55}Mo_{0.05}O_4$ visibly increases compared with the pristine $LiNi_{0.5}Mn_{1.5}O_4$. Hence, $LiMn_{1.4}Ni_{0.55}Mo_{0.05}O_4$ has a higher energy density than that of $LiNi_{0.5}Mn_{1.5}O_4$. The reason may be that there is a higher amount of $Ni^{2+}$ in $LiMn_{1.4}Ni_{0.55}Mo_{0.05}O_4$ than that in $LiNi_{0.5}Mn_{1.5}O_4$, and then increase the discharge capacity and discharge plateau at 4.7 V. Fig. 6 shows the discharge curves of the pristine and the Mo-doped $LiMn_{1.5}Ni_{0.5}O_4$ cathode materials at the 80th cycles discharged 2 C rate. It can be seen that all materials show a loss of the 4.7 V plateau at high discharge rate. The reason may be that lithium ions are not allowed enough time to diffuse from the inside of the electrode to the surface, and then lead to a large electrochemical polarization. However, it can be found that $LiMn_{1.425}Ni_{0.5}Mo_{0.05}O_4$ also shows the higher discharge capacity and discharge plateau than those of pristine $LiNi_{0.5}Mn_{1.5}O_4$. Hence, Mo doping may increase the energy density of $LiNi_{0.5}Mn_{1.5}O_4$ even at high discharge rate.

In order to study the influence of doping $Mo^{6+}$ ions on the cyclability of $LiNi_{0.5}Mn_{1.5}O_4$, the rate capabilities for three samples are illustrated in Fig. 7. The cells were discharged at increasingly higher currents from 0.1 to 2 *C* rates at room temperature. Before discharge, each cell was charged at a constant current of 0.1 *C* to 4.95 V. An interesting thing is that the discharge capacity increases slightly in the initial stage and the electrode reaches a largest discharge capacity after several cycles, probably because the electrodes are not thoroughly wetted by the electrolyte. Once the intercalation and deintercalation process start, the volume of the electrode begins to expand and shrink, enabling the electrolyte to wet the powders more thoroughly. At higher rates, the capacity difference between the pristine $LiNi_{0.5}Mn_{1.5}O_4$ electrode and Mo-doped $LiNi_{0.5}Mn_{1.5}O_4$ electrodes progressively increased. For the $LiNi_{0.5}Mn_{1.5}O_4$ electrodes, the discharge capacity obviously decreased with increasing rate. The rapid decrease in capacity is likely due to the high doses of $Mn^{3+}$ ions in pristine $LiNi_{0.5}Mn_{1.5}O_4$. At the 2 *C* rate after 80 cycles, the discharge capacity was 68.5 mAh $g^{-1}$ for the pristine $LiNi_{0.5}Mn_{1.5}O_4$ material (53.9% of the capacity at 0.1 *C*), 107.4 mAh $g^{-1}$ for the $LiMn_{1.425}Ni_{0.5}Mo_{0.05}O_4$ material (82.1% at 0.1 C), and 122.7 mAh $g^{-1}$ for the $LiMn_{1.4}Ni_{0.55}Mo_{0.05}O_4$ material (90.5% at 0.1 *C*). This result indicates that the Mo doping improves the rate capability of $LiNi_{0.5}Mn_{1.5}O_4$ as well as its capability to store Li ions. The reason may be suggested as follows. Trace water impurity in the electrolyte would cause the liberation of acid HF through the decomposition of $LiPF_6$, when $LiPF_6$-based electrolyte was used. The chemical reactions were proposed as follows [27–29]:

$$LiPF_6 + H_2O \rightarrow LiF + 2HF + POF_3 \quad (3)$$

$$POF_3 + H_2O \rightarrow PO_2F_2^- + HF + H^+ \quad (4)$$

$$PO_2F_2^- + H_2O \rightarrow PO_3F^{2-} + HF + H^+ \quad (5)$$

$$PO_3F^{2-} + H_2O \rightarrow PO_4^{3-} + HF + H^+ \quad (6)$$

In addition, the reactive $POF_3$ in the electrolyte reacts with carbonate solvents, such as EC, EMC, and DMC, to produce $CO_2$ and $OPF_2ORF$ [30]. This kind of reaction may destroy the SEI film during cycling. In fact, $LiPF_6$ itself contains a small amount of HF during the manufacturing process [31], and the salt can easily react with water, which unavoidably exists with very low concentration in the electrolyte, as shown in the following reaction equations [31–33]:

$$LiPF_6 \rightarrow LiF + PF_5 \quad (7)$$

$$PF_5 + H_2O \rightarrow 2HF + PF_3O \quad (8)$$

$$PF_5 + 2xe + 2xLi^+ \rightarrow xLiF + Li_xPF_{5-x} \quad (9)$$

$$PF_3O + 2xe + 2xLi^+ \rightarrow xLiF + Li_xPF_{3-x}O \quad (10)$$

$$PF_6^- + 2e + 3Li^+ \rightarrow 3LiF + PF_3 \quad (11)$$

HF will dissolve manganese based on Hunter's mechanism [34]:

$$4H^+ + 2LiMn^{3+}Mn^{4+}O_4 \rightarrow 3\lambda\text{–}MnO_2 + Mn^{2+} + 2Li^+ + 2H_2O \quad (12)$$

From these reactions, it can be found that acid is self-catalytic, and HF was regenerated by the reaction of water with $LiPF_6$ [35]. Hence, it can be concluded that the reduced content of Mn in our designed $LiMn_{1.425}Ni_{0.5}Mo_{0.05}O_4$ and $LiMn_{1.4}Ni_{0.55}Mo_{0.05}O_4$ samples can decrease the dissolution of manganese, and then increase the structure stability and rate performance during cycling. Furthermore, the relatively small powder morphology of

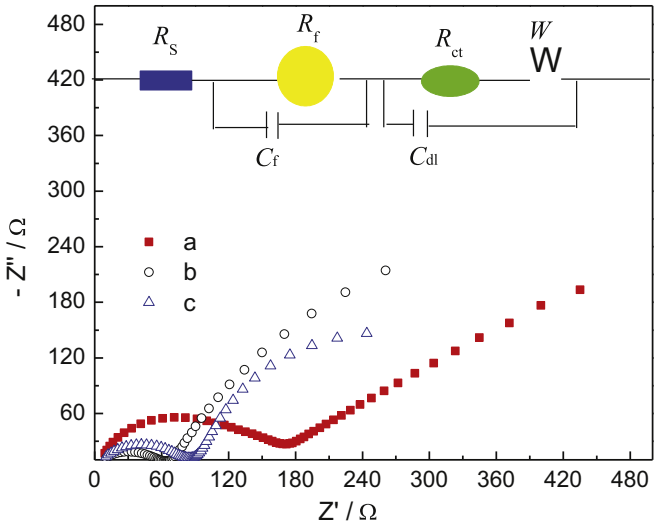


**Fig. 9.** Nyquist plots of the pristine and the Mo-doped $LiMn_{1.5}Ni_{0.5}O_4$ cathode materials (Inset is the equivalent circuit) (a) $LiMn_{1.5}Ni_{0.5}O_4$; (b) $LiMn_{1.425}Ni_{0.5}Mo_{0.05}O_4$; (c) $LiMn_{1.4}Ni_{0.55}Mo_{0.05}O_4$.

$LiMn_{1.4}Ni_{0.55}Mo_{0.05}O_4$ (see Fig. 3c) would help to release the stresses generated by the repetitive $Li^+$ intercalation, which can also improve rate capacity. Rate capability limitations result from a number of factors including low ionic and electronic conductivity of the electrode materials and slow insertion/extraction of lithium ions into the cathode, at the cathode/electrolyte interface [36]. Hence, the high rate cyclability is an important factor to be studied for future application of lithium batteries for EV, HEV and PHEV. $LiMn_{1.4}Ni_{0.55}Mo_{0.05}O_4$ cathode exhibits the best cycle performance among all samples even at high discharge rates, indicating possibility as a candidate of cathode material for lithium-ion batteries. Therefore, the high rate capacity together with good high rate cycling performance of the prepared $LiMn_{1.4}Ni_{0.55}Mo_{0.05}O_4$ material make it a promising alternative to next generation lithium-ion batteries.

Fig. 8 presents typical steady-state cyclic voltammograms (CVs) of pristine and Mo-doped $LiNi_{0.5}Mn_{1.5}O_4$ obtained at a scan rate of 0.2 mV $s^{-1}$. The broad oxidation peaks at about 4.05 V (anodic delithiation) and the reduction peak at 3.94 V (cathodic lithiation) can be attributed solely to the successive oxidation/reduction reactions of the $Mn^{3+}/Mn^{4+}$ couple in the spinel structure, compensated by lithium deinsertion–insertion [37]. The redox peaks of $LiNi_{0.5}Mn_{1.5}O_4$ with and without Mo doping located near 4.7 V are mainly ascribed to the two-step oxidation/reduction of $Ni^{2+}/Ni^{3+}$ and $Ni^{3+}/N^{i4+}$ [38,39]. The voltage differences between anodic and cathodic peaks reflect the polarization degree of the electrode. It can be observed that the Mo-doped $LiNi_{0.5}Mn_{1.5}O_4$ electrodes have lower potential differences than the pristine $LiNi_{0.5}Mn_{1.5}O_4$, which indicate that Mo-doping is favorable for reducing the electrode polarization. This also suggests Mo-doped $LiNi_{0.5}Mn_{1.5}O_4$ electrodes have faster lithium insertion/extraction kinetics during cycling. This observation confirms that the Mo doping enhances the reversibility of the $LiNi_{0.5}Mn_{1.5}O_4$, and then exhibits reversibility and good rate capability.

EIS is a useful tool to analyze the charge transfer process and electrode kinetics [40–42]. Fig. 9 shows the Nyquist plots of the pristine and the Mo-doped $LiMn_{1.5}Ni_{0.5}O_4$ cathode materials. It is clear from the figure that each spectrum consists of three parts. The semicircle at high frequencies reflects the resistance for $Li^+$ migration through the surface film ($R_f$) and film capacitance ($C_f$) [43,44], whereas the semicircle at medium to lower frequencies

**Table 1**
Fitted results from EIS.

| Sample | $R_{ct}/\Omega$ | $R_f/\Omega$ | $D_{Li}/cm^2\ s^{-1}$ |
|---|---|---|---|
| $LiNi_{0.5}Mn_{1.5}O_4$ | 1964 | 147.2 | $4.94 \times 10^{-16}$ |
| $LiNi_{0.5}Mn_{1.425}Mo_{0.05}O_4$ | 730.3 | 65.9 | $5.79 \times 10^{-16}$ |
| $LiNi_{0.55}Mn_{1.4}Mo_{0.05}O_4$ | 607.6 | 85.64 | $8.91 \times 10^{-16}$ |

represents the charge-transfer resistance ($R_{ct}$) and interfacial capacitance between the electrolyte and electrodes ($C_{dl}$). The low-frequency straight line can be attributed to diffusion of $Li^+$ ions in the samples [45]. The EIS spectra could be fitted by the equivalent circuit inserted in Fig. 9, which can explain the impedance spectra through the electrolyte resistance $R_S$, resistance of a solid electrolyte interface (SEI) film ($R_f$), capacitance of an SEI film ($C_f$) and Warburg impedance of solid-phase diffusion ($W$). The parameters of the equivalent circuit by computer simulations are shown in Table 1. Apparently, the charge-transfer resistance of the as-prepared Mo-doped $LiNi_{0.5}Mn_{1.5}O_4$ is much smaller than that of pure $LiNi_{0.5}Mn_{1.5}O_4$, in agreement with the small potential polarization shown in Fig. 7. It means that the Mo doping obviously decreases the charge-transfer resistance, further confirming the doping can improve the high rate performance. As reported by some references [46,47], EIS can be used to compare the size of the electronic conductivity. The smaller charge-transfer resistance of Mo-doped $LiNi_{0.5}Mn_{1.5}O_4$ indicates a larger electronic conductivity than that of pristine $LiNi_{0.5}Mn_{1.5}O_4$. Therefore, the high rate capability of active materials can be improved by constructing the new doping structure. According to the SEI film model principle, the relation between $R_f$ and SEI film conductivity $\rho$ is as follows [48]:

$$l = \frac{R_f S}{\rho} \tag{13}$$

where $l$ is the thickness of SEI film, and $S$ is the surface area of the electrode. Suppose the change of $\rho$ and $S$ is very little during the first processes of deintercalation of $Li^+$ for the $LiNi_{0.5}Mn_{1.5}O_4$ cathode material, which explains that the thickness of SEI film decreases due to the Mo doping. Hence, it may be concluded that the Mo doping $LiNi_{0.5}Mn_{1.5}O_4$ cathodes have higher lithium diffusion coefficient.

The diffusion coefficient of $Li^+$ ($D_{Li}$) can be calculated, based on the equation expressed as [49,50]

$$D_{Li} = \frac{R^2T^2}{2A^2n^4F^4C_{Li}^2\sigma^2} \tag{14}$$

where $R$ is the gas constant, $T$ the absolute temperature, $A$ the surface area of the cathode, $n$ the number of electrons transferred in the half-reaction for the redox couple, $F$ the Faraday constant, $C_{Li}$ the concentration of lithium ion in solid, and $\sigma$ is the Warburg factor, which is relative to $Z_{re}$-$\sigma$ can be obtained from the slope of the lines in Fig. 10.

$$Z_{re} = R_{ct} + R_s + \sigma\omega^{-\frac{1}{2}} \tag{15}$$

Based on the following equation, the diffusion coefficient of $Li^+$ in the electrode can be calculated as given in Table 1. It is obvious that the lithium diffusion coefficients increase due to the Mo doping. This result clearly indicates that the lithium-ion mobility of $Li_4Ti_5O_{12}$ can be effectively improved by moderate Mo doping. As we know, the discharge rate significantly affects discharge capacity. The diffusion overpotential is lower than the charge-transfer overpotential at low discharge current densities but becomes more dominant at higher current densities [51]. The reason is that

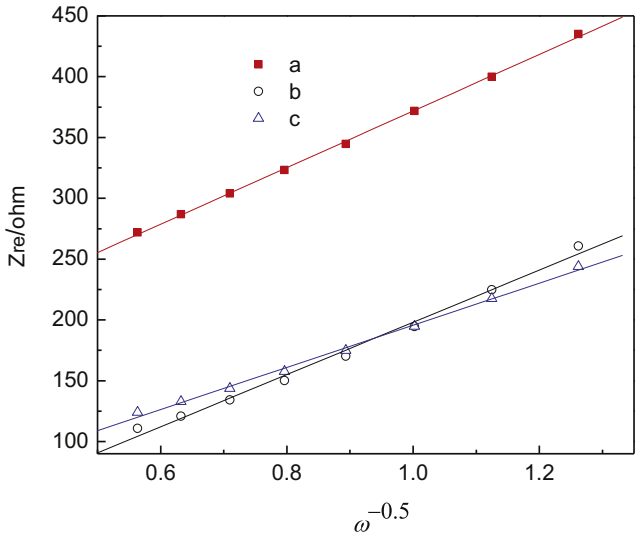


**Fig. 10.** Graph of $Z_{re}$ plotted against $\omega^{-1/2}$ at low frequency region for (a) $LiMn_{1.5}Ni_{0.5}O_4$; (b) $LiMn_{1.425}Ni_{0.5}Mo_{0.05}O_4$; (c) $LiMn_{1.4}Ni_{0.55}Mo_{0.05}O_4$.

lithium ions are allowed enough time to diffuse from the inside of the electrode to the surface during low discharge current. Hence, it can be concluded that charge-transfer resistance is the control step at low rate discharge. From Fig. 6, it can be seen that Mo-doped $LiMn_{1.5}Ni_{0.5}O_4$ cathodes have higher discharge capacity than that of pristine $LiMn_{1.5}Ni_{0.5}O_4$ at low rates discharge (0.1 and 0.5 *C*) due to the lower charge-transfer resistance. High-rate discharge ability is mainly controlled by the diffusion behavior rather than by the charge-transfer reaction [52,53]. From Fig. 7, it can be also seen that Mo-doped $LiMn_{1.5}Ni_{0.5}O_4$ cathodes have higher discharge capacity than that of pristine $LiMn_{1.5}Ni_{0.5}O_4$ at high rates discharge (1 and 2 *C*) due to the higher lithium diffusion coefficient. $LiMn_{1.4}Ni_{0.55}Mo_{0.05}O_4$ cathode exhibits the lowest charge-transfer resistance and the highest lithium diffusion coefficient among all samples, indicating that it has a high discharge capacity during low and high discharge currents. In addition, it can be found that there is a higher content of $Mn^{3+}$ in $LiMn_{1.425}Ni_{0.5}Mo_{0.05}O_4$ than that in $LiMn_{1.4}Ni_{0.55}Mo_{0.05}O_4$ according to the area of $Mn^{4+}/Mn^{3+}$ peak as shown in Fig. 5. The dissolution of $Mn^{3+}$ can decrease the structure stability of $LiMn_{1.425}Ni_{0.5}Mo_{0.05}O_4$ during cycling. It can be further proved $LiMn_{1.4}Ni_{0.55}Mo_{0.05}O_4$ shows the highest rate performance among all sample. These comments are well consistent with the charge–discharge results mentioned above. It should be highlighted that the as-prepared $LiMn_{1.4}Ni_{0.55}Mo_{0.05}O_4$ shows a potential advantage in response to the increasing demands for high power battery applications.

## 4. Conclusions

Good-quality Mo-doped $LiNi_{0.5}Mn_{1.5}O_4$ cathodes were successfully synthesized by the citric-acid-assisted sol–gel method. The reduced content of Mn in our designed $LiMn_{1.425}Ni_{0.5}Mo_{0.05}O_4$ and $LiMn_{1.4}Ni_{0.55}Mo_{0.05}O_4$ samples can decrease the dissolution of manganese, and then increase the structure stability and rate performance during cycling. The lower potential differences of Mo-doped $LiNi_{0.5}Mn_{1.5}O_4$ cathodes suggest that Mo-doped $LiNi_{0.5}Mn_{1.5}O_4$ electrodes have faster lithium insertion/extraction kinetics than that of pristine $LiNi_{0.5}Mn_{1.5}O_4$ during cycling. Moreover, it is further demonstrated from EIS that the charge-transfer resistance of the Mo-doped $LiNi_{0.5}Mn_{1.5}O_4$ is much smaller than that of pristine $LiNi_{0.5}Mn_{1.5}O_4$. Correspondingly, the high rate discharge capability of the Mo-doped $LiNi_{0.5}Mn_{1.5}O_4$ is obtained based on the fast surface charge-transfer reaction, the reduced charge transfer resistance and the increased lithium ion diffusion. Therefore, the high rate capability and good cycle stability of active materials can be greatly improved by doping. In addition, $LiMn_{1.4}Ni_{0.55}Mo_{0.05}O_4$ cathode exhibits the smallest particle size, the lowest charge-transfer resistance and the highest lithium diffusion coefficient among all samples, indicating that it has a high reversibility and good rate capability. Hence, Mo doping is an effective way to improve the electrochemical performance of $LiNi_{0.5}Mn_{1.5}O_4$. The same strategy adopted in this work could be helpful to explore and develop desired cathode materials for advanced lithium-ion batteries.

## Acknowledgments

This work was financially supported by the National Natural Science Foundation of China (no. 51274002), the China Postdoctoral Science Foundation (no. 2012M520749), the Zhejiang Postdoctoral Preferential Foundation (no. Bsh1201013), the Program for Innovative Research Team in Anhui University of Technology (no. TD201202), and the Scientific Research Foundation of Graduate School of Anhui University of Technology (no. 2012032).

## References

[1] J. Yang, S.-C. Wang, X.-Y. Zhou, J. Xie, Int. J. Electrochem. Sci. 7 (2012) 6118–6126.
[2] Y.-K. Sun, B.-R. Lee, H.-J. Noh, H. Wu, S.-T. Myungd, K. Amine, J. Mater. Chem. 21 (2011) 10108–10112.
[3] X. Zhou, J. Tang, J. Yang, J. Xie, B. Huang, J. Mater. Chem. A 1 (2013) 5037–5044.
[4] M. Armand, J.M. Tarascon, Nature 451 (2008) 652–657.
[5] J. Yao, L. Lv, C. Shen, P. Zhang, K.-F. Aguey-Zinsou, L. Wang, Ceram. Int. 39 (2013) 3359–3364.
[6] C. Wang, S. Lu, S. Kan, J. Pang, W. Jin, X. Zhang, J. Power Sources 189 (2009) 607–610.
[7] D.H. Jang, Y.J. Shin, S.M. Oh, J. Electrochem. Soc. 143 (1996) 2204–2211.
[8] Y.Y. Xia, Y.H. Zhou, M. Yoshio, J. Electrochem. Soc. 144 (1997) 2593–2600.
[9] H.-C. Wang, C.-H. Lu, J. Power Sources 119–121 (2003) 738–742.
[10] C.H. Shen, R.S. Liu, R. Gundakaram, J.M. Chen, S.M. Huang, J.S. Chen, C.M. Wang, J. Power Sources 102 (2001) 21–28.
[11] M.W. Raja, S. Mahanty, R.N. Basu, J. Power Sources 192 (2009) 618–626.
[12] J.-F. Lee, Y.-W. Tsai, R. Santhanam, B.J. Hwang, M.-H. Yang, D.-G. Liu, J. Power Sources 119–121 (2003) 721–726.
[13] E. Lee, K.A. Persson, Energy Environ. Sci. 5 (2012) 6047–6051.
[14] G.Q. Liu, L. Wen, Y.M. Liu, J. Solid State Electrochem. 14 (2010) 2191–2202.
[15] C. Locati, U. Lafont, L. Simonin, F. Ooms, E.M. Kelder, J. Power Sources 174 (2007) 847–851.
[16] G.Q. Liu, L. Wen, G.Y. Liu, Y.W. Tian, J. Alloys Compd. 501 (2010) 233–235.
[17] D. Li, A. Ito, K. Kobayakawa, H. Noguchi, Y. Sato, J. Power Sources 161 (2006) 1241–1246.
[18] G.T.-K. Fey, C.-Z. Lu, T.P. Kumar, J. Power Sources 115 (2003) 332–345.
[19] H. Wang, H. Xia, M.O. Lai, L. Lu, Electrochem. Commun. 11 (2009) 1539–1542.
[20] T.-F. Yi, Y. Xie, Y.-R. Zhu, R.-S. Zhu, M.-F. Ye, J. Power Sources 211 (2012) 59–65.
[21] X.X. Xu, J. Yang, Y.Q. Wang, Y.N. NuLi, J.L. Wang, J. Power Sources 174 (2007) 1113–1116.
[22] Y.-K. Sun, S.W. Oh, C.S. Yoon, H.J. Bang, J. Prakash, J. Power Sources 161 (2006) 19–26.
[23] P. Strobel, J. Tillier, A. Diaz, A. Ibarra-Palos, F. Thiery, J.B. Soupart, J. Power Sources 174 (2007) 910–915.
[24] X. Nie, B. Zhong, M. Chen, K. Yin, L. Li, H. Liu, X. Guo, Electrochim. Acta 97 (2013) 184–191.
[25] S.S. Zhang, K. Xu, T.R. Jow, J. Electrochem. Soc. 149 (2002) A1521–A1526.
[26] H. Miyashiro, S. Seki, Y. Kobayashi, Y. Ohno, Y. Mita, A. Usami, Electrochem. Commun. 7 (2005) 1083–1086.
[27] D. Aurbach, J. Power Sources 89 (2000) 206–218.
[28] E. Wang, D. Ofer, W. Bowden, N. Iltchev, R. Moses, K. Brandt, J. Electrochem. Soc. 147 (2000) 4023–4028.
[29] L. Yang, M. Takahashi, B. Wang, Electrochim. Acta 51 (2006) 3228–3234.
[30] C.L. Campion, W. Li, B.L. Lucht, J. Electrochem. Soc. 152 (2005) A2327–A2334.
[31] G.G. Amatucci, A. Blyr, C. Sigala, P. Alfonse, J.M. Tarascon, Solid State Ionics 104 (1997) 13–25.
[32] D. Aurbach, Y. Ein-Eli, O. Chusid, Y. Carmeli, M. Babai, H. Yamin, J. Electrochem. Soc. 141 (1994) 603–611.

[33] D. Aurbach, B. Markovsky, A. Shechter, Y. Ein-Eli, H. Cohen, J. Electrochem. Soc. 143 (1996) 3809–3820.
[34] J.C. Hunter, J. Solid State Chem. 39 (1981) 142–147.
[35] A. Blyr, C. Sigala, G. Amatucci, D. Guyomard, Y. Chabre, J.M. Tarascon, J. Electrochem. Soc. 145 (1998) 194–209.
[36] R. Santhanam, B. Rambabu, J. Power Sources 195 (2010) 4313–4317.
[37] S.H. Oh, S.H. Jeon, W.I. Cho, C.S. Kim, B.W. Cho, J. Alloys Compd. 452 (2008) 389–396.
[38] T. Yang, N. Zhang, Y. Lang, K. Sun, Electrochim. Acta 56 (2011) 4058–4064.
[39] B. Markovsky, Y. Talyossef, G. Salitra, D. Aurbach, H.-J. Kim, S. Choi, Electrochem. Commun. 6 (2004) 821–826.
[40] X.-Y. Zhou, J.-J. Tang, J. Yang, Y.-l. Zou, S.-c. Wang, J. Xie, L.-l. Ma, Electrochim. Acta 70 (2012) 296–303.
[41] X. Zhou, Y. Zou, J. Yang, J. Solid State Chem. 198 (2013) 231–237.
[42] H. Ma, S.Y. Zhang, W.Q. Ji, Z.L. Tao, J. Chen, J. Am. Chem. Soc. 130 (2008) 5361–5367.
[43] M.D. Levi, D. Aurbach, J. Phys. Chem. B 101 (1997) 4630–4640.
[44] M.D. Levi, E.A. Levi, D. Aurbach, J. Electroanal. Chem. 421 (1997) 89–97.
[45] G.G. Wang, J.M. Wang, W.Q. Mao, H.B. Shao, J.Q. Zhang, C.N. Cao, J. Solid State Electrochem. 9 (2005) 524–530.
[46] J. Lee, P. Kumar, B.M. Moudgil, R.K. Singh, Solid State Ionics 231 (2013) 18–24.
[47] Q. Zhang, C. Zhang, B. Li, S. Kang, X. Li, Y. Wang, Electrochim. Acta 9 (2013) 146–152.
[48] T.-F. Yi, C.-Y. Li, Y.-R. Zhu, R.-S. Zhu, J. Shu, Russ. J. Electrochem. 46 (2010) 227–232.
[49] G.Q. Liu, H.T. Kuo, R.S. Liu, C.H. Shen, D.S. Shy, X.K. Xing, J.M. Chen, J. Alloys Compd. 496 (2010) 512–516.
[50] S.-L. Chou, J.-Z. Wang, H.-K. Liu, S.-X. Dou, J. Phys. Chem. C 115 (2011) 16220–16227.
[51] M.-S. Wu, P.-C.J. Chiang, J.-C. Lin, J. Electrochem. Soc. 152 (2005) A47–A52.
[52] M. Geng, J. Han, F. Feng, D.O. Northwood, J. Electrochem. Soc. 146 (1999) 3591–3595.
[53] M.S. Wu, H.R. Wu, Y.Y. Wang, C.C. Wan, J. Appl. Electrochem. 33 (2003) 619–625.